On the Influence of Fluid-Structure-Interactions on the Static Stability of Thin Walled Shell Structures

M. Hassler and K. Schweizerhof
Universität Karlsruhe, Institut für Mechanik

On the Influence of Fluid-Structure-Interaction on the Static Stability of Thin Walled Shell Structures

M. Haßler and K. Schweizerhof

November 30, 2006

Abstract

The purpose of this contribution is to investigate the stabilizing influence of hydrostatic fluid and/or gas pressure supports (especially the effect of the volume dependence of gas or fluid pressures) on the stability, here the eigenvalues and eigenmodes of the stiffness matrix of shell or membrane-like structures undergoing large displacements. For this purpose an analytical mesh free or lumped parameter description for the fluid/gas (see also [3], [11], [12] and [13]) is taken, which yields a special structure of the nonlinear equations representing the change of the gas or fluid volume or alternatively the change of the wetted part of the shell surface. Finally this procedure leads to a stiffness matrix matrix updated with several rank updates – depending on the volume containing either gas or fluid or both. These rank updates are a key part in the stability analysis: They describe the different coupling of the fluid or gas volume change with the structural displacements in addition to the deformation dependence of the standard pressure. The specific rank updates allow the derivation of a very efficient algorithm to compute the modifications of the eigenvalues and eigenmodes of the original stiffness matrix without gas or fluid loading or support.

Keywords: fluid-structure-interaction; large displacements; volume dependence; stability; finite elements

1 Introduction

In conventional finite element analyses of structures with closed volumes an internal pressure is assumed, which is acting normal to the surface of the system. For relatively small deformations and structures not prone to instability this approximation is adequate. However, for stability problems further effects have to be considered, especially the change of the volume and the inner state variables of the gas and/or the fluid. The fact that the applied gas or fluid pressure is volume dependent is often neglected as also for example the volume dependence of the current fluid level. For early investigations of buckling of structures with internal pressure we refer to Fung/Sechler [6] and Harris et al. [8].

This contribution is devoted to the investigations of the influence of such a deformation dependent fluid/gas support or loading on the eigenvalues and eigenmodes of the stiffness matrix of thin walled shell structures undergoing large displacements. For this purpose we refer to the former contributions of the authors group [11], [12], [13]. The contributions of Berry et al. [2] and Bonet et al. [3] were focusing only on gas supported resp. loaded shell and membrane type structures. With the derivations given in [11], [12] and [13] it is possible to come up with an analytical

formulation of the fluid/gas terms only described by surface integrals over the surrounding wetted structure. Hence e.g no FE discretization of the fluid or the gas is necessary. Already van Dijk et al. [4] proposed a FE-description for shells filled with a combination of gas and fluid. However, the effect of of the change of the normals and effect of the hydrostatic pressure were neglected and some approximations towards the fluid compressibility have been made. Only the deformation behavior of airsprings and bottles was considered. A further contribution of the authors group [9] recently submitted for publication merges all previous developments and thus provides a unified formulation for closed chambers containing any combination of volume dependent loading and support (see Fig. 1.1) and allows any combinations of multiple chambers, too.
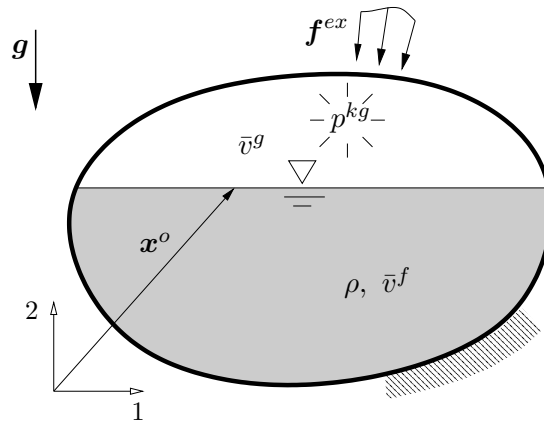

Fig. 1.1: Elastic shell structure filled with fluid and gas

Due to the fact that in [9] the linearized set of equations – featuring several dyadic rank updates of the stiffness matrix – for fluid and/or gas supported membrane structures has already been derived, it will be only briefly presented here. The specific rank updates of the stiffness matrix are a main part in the stability investigation, because they allow the derivation of a very efficient algorithm to determine the influence of the fluid or gas loading on the eigenvalues and eigenmodes of the stiffness matrix. The numerical examples contain fluid and gas filled shell structures with rather thin flexible walls investigated for buckling. The performance of the efficient derived algorithm is also discussed.

2   Eigenvalue Analysis

As shown in the previous works of the authors group [11], [12], [13] the volume dependence of the inner state variables (e.g. pressure p, fluid densitiy ρ or fluid level x^o) leads to several rank updates of the global stiffness matrix $\boldsymbol{K}$. For reasons of simplicity the special case of a single chamber only loaded with gas will serve as an example. Keeping the notation introduced in [9], for a system only loaded with gas the linearized set of equations describing the equilibrium becomes

$$\left(\boldsymbol{K} + \alpha_t \boldsymbol{a}\boldsymbol{a}^T\right)\boldsymbol{d} = \boldsymbol{f}\ , \quad \text{with} \quad \boldsymbol{K} = \boldsymbol{K}^{el} + \boldsymbol{K}^g\ , \tag{2.1}$$

where $\boldsymbol{d}$ is the unknown nodal displacement vector, $\boldsymbol{K}^{el}$ the stiffness part of e.g. the elastic shell structure and $\boldsymbol{K}^g$ the so-called load-stiffness matrix [15] reflecting the

normal change of the gas pressure loading. The external forces and the residuals of both the virtual work of the inner forces of the elastic structure and the virtual work of the pressure loading $\boldsymbol{f}^g$ are combined in the right hand side vector $\boldsymbol{f}$. The volume dependence of the internal gas pressure $p^{kg} = p^{kg}(\bar{v}^g)$ leads to the rank update with the coupling vector $\boldsymbol{a}$, which can be interpreted as the volume change of the enclosed gas. The constant pressure volume gradient α_t couples the volume change with the pressure change. The formulae for the computation of $\boldsymbol{K}^g$, $\boldsymbol{f}^g$, $\boldsymbol{a}$ and α_t are given in the appendix. This dyadic rank update results in a fully populated part of the system matrix $\boldsymbol{A} = \boldsymbol{K} + \alpha_t \boldsymbol{a}\boldsymbol{a}^T$, which may lead to fairly high numerical effort during the modal decomposition process. To bypass the solution with such an almost fully populated system matrix in a first step the standard eigenvalue problem

$$\boldsymbol{K}\,\boldsymbol{\psi}_i = \lambda_i\,\boldsymbol{\psi}_i \tag{2.2}$$

has to be solved. With conventional algorithms, as for example a subspace iteration method, the eigenvalues λ_i and the eigenvectors $\boldsymbol{\psi}_i$ of the matrix $\boldsymbol{K}$ having the structure of a standard structural matrix can be computed. In the next step the effect of the dyadic update of $\boldsymbol{K}$ by the coupling vectors on the eigenvalues and -vectors will be investigated.

2.1 Computation of Shifted Eigenvalues

Starting from the standard eigenvalue problem

$$\boldsymbol{A}\,\boldsymbol{\phi}_i = \chi_i\,\boldsymbol{\phi}_i \tag{2.3}$$

for the volume coupled system matrix $\boldsymbol{A}$, the modal vectors $\boldsymbol{\phi}_i$ can be assembled in the modal matrix $\boldsymbol{\Phi}$ and the associated eigenvalues χ_i in the spectral matrix $\boldsymbol{X}$. Rearranging equation (2.3) then leads to

$$\boldsymbol{A}\boldsymbol{\Phi} = \boldsymbol{\Phi}\boldsymbol{X}\ . \tag{2.4}$$

Subsequently the modal matrix $\boldsymbol{\Phi}$ can be split up into a modal factor matrix $\boldsymbol{\Xi}$ and the modal matrix $\boldsymbol{\Psi}$, which contains all eigenvectors $\boldsymbol{\psi}_i$ of the uncoupled stiffness matrix $\boldsymbol{K}$. Thus $\boldsymbol{\Phi}$ can be written as:

$$\boldsymbol{\Phi} = \boldsymbol{\Psi}\boldsymbol{\Xi} = \boldsymbol{\Psi} \begin{pmatrix} | & | & & | & & | \\ \boldsymbol{\xi}_1 & \boldsymbol{\xi}_2 & \cdots & \boldsymbol{\xi}_i & \cdots & \boldsymbol{\xi}_n \\ | & | & & | & & | \end{pmatrix} \tag{2.5}$$

All modal vectors are normalized, thus

$$\boldsymbol{\Psi}^T\boldsymbol{\Psi} = \boldsymbol{I}\ . \tag{2.6}$$

Inserting equation (2.5) in (2.4) and left hand multiplication with $\boldsymbol{\Psi}^T$ yields

$$\begin{aligned} \boldsymbol{\Psi}^T \cdot | \quad \boldsymbol{A}\boldsymbol{\Psi}\boldsymbol{\Xi} &= \boldsymbol{\Psi}\boldsymbol{\Xi}\boldsymbol{X} \\ \boldsymbol{\Psi}^T\boldsymbol{A}\boldsymbol{\Psi}\boldsymbol{\Xi} &= \boldsymbol{\Psi}^T\boldsymbol{\Psi}\boldsymbol{\Xi}\boldsymbol{X} \\ \boldsymbol{\Psi}^T\boldsymbol{A}\boldsymbol{\Psi}\boldsymbol{\Xi} &= \boldsymbol{\Xi}\boldsymbol{X}\ . \end{aligned} \tag{2.7}$$

With the notation

$$\boldsymbol{A}^\star = \boldsymbol{\Psi}^T\boldsymbol{A}\boldsymbol{\Psi} = \boldsymbol{\Psi}^T\left(\boldsymbol{K} + \alpha_t\boldsymbol{a}\boldsymbol{a}^T\right)\boldsymbol{\Psi}\ . \tag{2.8}$$

a modified form of the eigenvalue problem (2.4) is obtained

$$A^\star \Xi = \Xi X \ , \tag{2.9}$$

which can be rewritten for the columns $\boldsymbol{\xi}_i$ of the modal factor matrix $\boldsymbol{\Xi}$ and the eigenvalues χ_i:

$$A^\star \boldsymbol{\xi}_i = \chi_i \ \boldsymbol{\xi}_i \ . \tag{2.10}$$

Substituting (2.8) into (2.10) results after some reordering in:

$$\begin{aligned}
\left(\boldsymbol{\Psi}^T \left[\boldsymbol{K} + \alpha_t \boldsymbol{a} \boldsymbol{a}^T \right] \boldsymbol{\Psi} - \chi_i \boldsymbol{I} \right) \boldsymbol{\xi}_i &= \boldsymbol{0} \\
\left(\boldsymbol{\Psi}^T \boldsymbol{K} \boldsymbol{\Psi} + \alpha_t \boldsymbol{\Psi}^T \boldsymbol{a} \boldsymbol{a}^T \boldsymbol{\Psi} - \chi_i \boldsymbol{I} \right) \boldsymbol{\xi}_i &= \boldsymbol{0} \ .
\end{aligned} \tag{2.11}$$

Using the spectral matrix $\boldsymbol{\Lambda}$ of $\boldsymbol{K}$

$$\boldsymbol{\Lambda} = \boldsymbol{\Psi}^T \boldsymbol{K} \boldsymbol{\Psi} \tag{2.12}$$

along with the modified coupling vector

$$\bar{\boldsymbol{a}} = \boldsymbol{\Psi}^T \boldsymbol{a} \tag{2.13}$$

yields

$$\left(\boldsymbol{\Lambda} + \alpha_t \bar{\boldsymbol{a}} \bar{\boldsymbol{a}}^T - \chi_i \boldsymbol{I} \right) \boldsymbol{\xi}_i = \boldsymbol{0} \ . \tag{2.14}$$

For this homogeneous set of equations non-trivial solutions $\boldsymbol{\xi}_i \neq \boldsymbol{0}$ do exist, if the determinant of the coefficient matrix $\left(\boldsymbol{\Lambda} + \bar{\boldsymbol{a}} \bar{\boldsymbol{a}}^T - \chi_i \boldsymbol{I} \right)$ vanishes.

$$det \left\{ \boldsymbol{\Lambda} + \alpha_t \bar{\boldsymbol{a}} \bar{\boldsymbol{a}}^T - \chi_i \boldsymbol{I} \right\} = 0 \tag{2.15}$$

Now two cases concerning the coordinates $\bar{a}_j$ must be considered:

2.1.1   Case 1: All coordinates unequal zero $(\bar{a}_j \neq 0)$

In this case all new eigenvalues are different from the old ones: $\chi_i \neq \lambda_i$. This ensures the matrix $(\boldsymbol{\Lambda} - \chi_i \boldsymbol{I})$ not to be singular. Therefore it can be moved out of the operand in equation (2.15).

$$det \left\{ (\boldsymbol{\Lambda} - \chi_i \boldsymbol{I}) \left(\boldsymbol{I} + \alpha_t \left[\boldsymbol{\Lambda} - \chi_i \boldsymbol{I} \right]^{-1} \bar{\boldsymbol{a}} \bar{\boldsymbol{a}}^T \right) \right\} = 0 \tag{2.16}$$

Using the multiplication rule of determinants on equation (2.16) results in

$$det \left(\boldsymbol{\Lambda} - \chi_i \boldsymbol{I} \right) \ det \left(\boldsymbol{I} + \alpha_t \left[\boldsymbol{\Lambda} - \chi_i \boldsymbol{I} \right]^{-1} \bar{\boldsymbol{a}} \bar{\boldsymbol{a}}^T \right) = 0 \ . \tag{2.17}$$

The determinant of the rank-one-updated identity matrix $\boldsymbol{I}$ can be easily given as

$$det \left(\boldsymbol{I} + \alpha_t \left[\boldsymbol{\Lambda} - \chi_i \boldsymbol{I} \right]^{-1} \bar{\boldsymbol{a}} \bar{\boldsymbol{a}}^T \right) = 1 + \alpha_t \bar{\boldsymbol{a}}^T \left[\boldsymbol{\Lambda} - \chi_i \boldsymbol{I} \right]^{-1} \cdot \bar{\boldsymbol{a}} \ , \tag{2.18}$$

see [14]. Thus the following conditional equation for the eigenvalues χ_i is obtained:

$$det \left(\boldsymbol{\Lambda} - \chi_i \boldsymbol{I} \right) \left(1 + \alpha_t \bar{\boldsymbol{a}}^T \left[\boldsymbol{\Lambda} - \chi_i \boldsymbol{I} \right]^{-1} \cdot \bar{\boldsymbol{a}} \right) = 0 \tag{2.19}$$

As the new eigenvalues are different from the old ones, $\chi_i \neq \lambda_i$, the determinant of the diagonal matrix $(\boldsymbol{\Lambda} - \chi_i \boldsymbol{I})$ is unequal zero. Consequently the second factor

in equation (2.19) must be identical to zero to ensure the existence of non-trivial solutions. For the eigenvalues χ_i the characteristical polynomial $p(\chi)$ is obtained:

$$p(\chi) = 1 + \alpha_t \bar{\boldsymbol{a}}^T \left[\boldsymbol{\Lambda} - \chi \boldsymbol{I} \right]^{-1} \cdot \bar{\boldsymbol{a}} = 0 \tag{2.20}$$

Because $(\boldsymbol{\Lambda} - \chi \boldsymbol{I})$ is a diagonal matrix, the polynomial $p(\chi)$ can be simplified by summing up the product of the reciprocals of the jth diagonal element with the square of the jth coordinate $\bar{a}_j$.

$$p(\chi) = 1 + \alpha_t \sum_{j=1}^{n} \frac{\bar{a}_j \bar{a}_j}{\lambda_j - \chi} = 0 \tag{2.21}$$

Function (2.21) has poles at the eigenvalues λ_i of the stiffness matrix $\boldsymbol{K}$. Further on, function (2.21) has for a positive α_t the following limits between the poles (see also Fig. 2.1):

$$\lim_{\chi \to \lambda_j^+} = -\infty \ , \quad \lim_{\chi \to \lambda_{j+1}^-} = \infty \ , \quad \lim_{\chi \to -\infty} = 1 \quad \text{and} \quad \lim_{\chi \to \infty} = 1 \ . \tag{2.22}$$

The pressure volume gradient α_t can be physically seen as a kind of spring constant of the gas. Negative values for α_t are therefore artificial and physically not possible. A closer look at the definition

$$\alpha_t = \kappa \frac{p_t^{kg}}{\bar{v}_t^{g}} \quad \text{(with } \kappa = 1.4, \ \text{see [1])} \tag{2.23}$$

shows that neither negative volumes $\bar{v}_t^{g}$ nor negative pressures p_t^{kg} exist, thus $\alpha_t > 0$ always yields.

The characteristical polynomial $p(\chi)$ is strictly monotone between its poles, therefore the new eigenvalues χ_i resp. the zero values of $p(\chi)$, must lie somewhere in between the poles. As depicted in Fig. 2.1 the new eigenvalues χ_i will increase for a positive
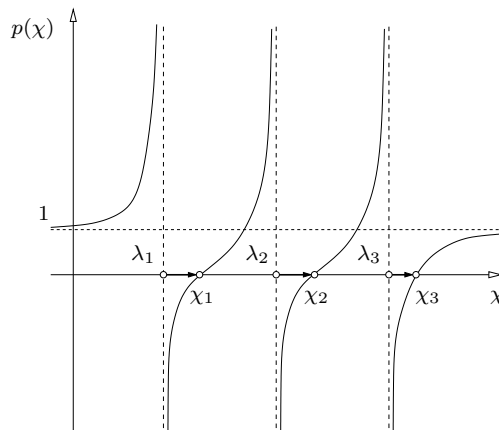
Fig. 2.1: Eigenvalue shift for the example of a 3rd order polynomial $p(\chi)$ and $\alpha_t > 0$

pressure volume gradient α_t, resp. a gas/fluid support.

$$\lambda_1 < \chi_1 < \lambda_2 < \chi_2 < ... < \lambda_n < \chi_n \tag{2.24}$$

As already mentioned the polynomial $p(\chi)$ is strictly monotone between the poles λ_j, therefore an efficient method to localize the zeroes in $p(\chi)$ can be found by the bisection method. For a given tolerance *tol*

$$n > log_2 \left(\frac{\lambda_{j+1} - \lambda_j}{tol} \right) \tag{2.25}$$

iterations are necessary to approximate the new eigenvalue χ_j [5].

2.1.2   Case 2: Coordinate $\bar{a}_j = 0$

Physically, the modified coupling vector $\bar{a}$ still represents the volume change of the structure. If a specific degree of freedom has no influence on the volume change, the associated coordinate $\bar{a}_j = 0$ of the coupling vector consequently will be zero. This means that the corresponding eigenvalue λ_j and eigenmode ϕ_j are not affected by the gas support and therefore will remain untouched. The mathematical interpretation of this fact is that in this case the matrix

$$\boldsymbol{\Lambda} + \alpha_t \bar{a} \bar{a}^T - \chi_i \boldsymbol{I} \tag{2.26}$$

contains zero entries in the jth row and the jth column, except for the diagonal element. This has the effect that the jth eigenvalue χ_j of (2.26) equals the old eigenvalue λ_j. Therefore in a first step, in the algorithm all zero entries must be filtered out of the coupling vector $\bar{a}$ and the associated rows and columns in the spectral matrix $\boldsymbol{\Lambda}$ must be reduced likewise. Thus we obtain a reduced coupling vector $\hat{a}$ without any zero entries and a reduced spectral matrix $\hat{\boldsymbol{\Lambda}}$ and can proceed in analogy to case 1 (2.21) with the characteristic polynomial $\hat{p}(\chi_i)$ of a reduced order

$$\hat{p}(\chi_i) = 1 + \sum_{j=1}^{m} \frac{\hat{a}_j \hat{a}_j}{\hat{\lambda}_j - \chi} = 0 , \qquad \text{with} \quad \chi \neq \lambda_j , \quad m < n . \tag{2.27}$$

2.2   Computation of Eigenvectors

For the computation of the corresponding eigenvectors equation (2.14) is considered again, focusing on the column $\boldsymbol{\xi}_i$ of the modal factor matrix $\boldsymbol{\Xi}$:

$$\left(\boldsymbol{\Lambda} + \alpha_t \bar{a} \bar{a}^T - \chi_i \boldsymbol{I} \right) \boldsymbol{\xi}_i = \boldsymbol{0} . \tag{2.28}$$

Rearranging this equation yields

$$
\begin{aligned}
(\boldsymbol{\Lambda} - \chi_i \boldsymbol{I}) \boldsymbol{\xi}_i &= -\alpha_t \left(\bar{a} \bar{a}^T \right) \boldsymbol{\xi}_i \\
(\boldsymbol{\Lambda} - \chi_i \boldsymbol{I}) \boldsymbol{\xi}_i &= -\alpha_t \bar{a} \left(\bar{a}^T \cdot \boldsymbol{\xi}_i \right) \\
\boldsymbol{\xi}_i &= -\alpha_t (\boldsymbol{\Lambda} - \chi_i \boldsymbol{I})^{-1} \bar{a} \left(\bar{a}^T \cdot \boldsymbol{\xi}_i \right) .
\end{aligned}
\tag{2.29}
$$

To eliminate the implicit form of $\boldsymbol{\xi}_i$ it can be normalized by its length, leading to

$$
\begin{aligned}
\boldsymbol{\xi}_i &= -\frac{\alpha_t (\boldsymbol{\Lambda} - \chi_i \boldsymbol{I})^{-1} \bar{a} \left(\bar{a}^T \cdot \boldsymbol{\xi}_i \right)}{|| \alpha_t (\boldsymbol{\Lambda} - \chi_i \boldsymbol{I})^{-1} \bar{a} \ (\bar{a}^T \cdot \boldsymbol{\xi}_i) ||} \\
&= -\frac{(\boldsymbol{\Lambda} - \chi_i \boldsymbol{I})^{-1} \bar{a}}{|| (\boldsymbol{\Lambda} - \chi_i \boldsymbol{I})^{-1} \bar{a} ||} .
\end{aligned}
\tag{2.30}
$$

as the ith column of $\boldsymbol{\Xi}$. With the multiplicative split (2.5) the transformed modal matrix can then be computed:

$$
\boldsymbol{\Phi} = \boldsymbol{\Psi}\boldsymbol{\Xi} = \boldsymbol{\Psi}
\begin{pmatrix}
| & | & & | & & | & \\
\boldsymbol{\xi}_1 & \boldsymbol{\xi}_2 & \cdots & \boldsymbol{\xi}_i & \cdots & \boldsymbol{\xi}_n & . \\
| & | & & | & & | &
\end{pmatrix}
\tag{2.31}
$$

In the case of zero entries in the coupling vector the reduced modal matrix $\hat{\boldsymbol{\Phi}}$, which can also be computed according to this outlined scheme, must be amended by the old eigenvectors corresponding to the zero entries of $\bar{\boldsymbol{a}}$ to make it complete.

2.3   Efficiency considerations

In most engineering problems only a few lower eigenvalues are of interest. But an obvious disadvantage in the presented algorithm is the fact that – although only a few eigenvalues χ_i and the associated eigenmodes ϕ_i of the system matrix $\boldsymbol{A}$ are to be computed – in a preceding computation both, all eigenvalues λ_j of the global stiffness matrix $\boldsymbol{K}$ are necessary to set up the characteristical polynomial $p(\chi)$ and the complete modal matrix $\boldsymbol{\Psi}$ of $\boldsymbol{K}$ with all its decoupled eigenvectors is also needed to obtain the new modal matrix $\boldsymbol{\Phi}$ via the product approach (2.31). In this section a reduction of the general case with all n eigenvalues and n eigenmodes of $\boldsymbol{K}$ is discussed and in which cases just $m < n$ lower ones are sufficient.

A central factor in the modal analysis within this scheme are the distances of the old eigenvalues λ_j among each other, because they determine the coupling. If all eigenvalues λ_{j+1} are much smaller than all following eigenvalues λ_{m+1}

$$
\lambda_{j+1} \ll \lambda_{m+1} \, ,
\tag{2.32}
$$

then we can conclude for the new eigenvalues χ_j with

$$
\lambda_j < \chi_j < \lambda_{j+1} \ll \lambda_{m+1}
\tag{2.33}
$$

that they are also much smaller than λ_{m+1}:

$$
\chi_j \ll \lambda_{m+1}
\tag{2.34}
$$

Therefore – although for the computation of the first $j = 1..m$ shifted eigenvalues χ_j in the strict sense all old eigenvalues $\lambda_1...\lambda_j...\lambda_n$ must be considered – all summands in the characteristical polynomial for $m + 1 \leq j \leq n$ are negligible compared to the rest. Thus we get under the assumption $\bar{a}_j \ll \lambda_{m+1}$ (verification of assumption at the end of section)

$$
\begin{aligned}
p(\chi) &= 1 + \alpha_t \sum_{j=1}^{m} \frac{\bar{a}_j \bar{a}_j}{\lambda_j - \chi} + \alpha_t \sum_{j=m+1}^{n} \frac{\bar{a}_j \bar{a}_j}{\lambda_j - \chi} = 0 \\
&\approx 1 + \alpha_t \sum_{j=1}^{m} \frac{\bar{a}_j \bar{a}_j}{\lambda_j - \chi} \, .
\end{aligned}
\tag{2.35}
$$

If the distance between the eigenvalues is large enough, then the updated lower eigenvalues χ_j remain almost unaffected by higher ones greater than λ_m. Thus both, the search for the old eigenvalues λ_j with conventional methods and the search for the zeroes in $p(\chi)$ with the bisection method can be restricted to a minimum number m, which may reduce the computational effort considerably for large FE-problems.

The same argument can be used to reduce the number of eigenvectors $\boldsymbol{\psi}_i$ of $\boldsymbol{K}$ necessary for the setup of the new modal matrix $\boldsymbol{\Phi}$. Looking at equation (2.30) again the non-normalized vector can be written as

$$
\boldsymbol{\xi}_i^\star = -\left(\boldsymbol{\Lambda} - \chi_i \boldsymbol{I}\right)^{-1} \bar{\boldsymbol{a}} \qquad = -\begin{bmatrix} \bar{a}_1 / \left(\lambda_1 - \chi_i\right) \\ \bar{a}_2 / \left(\lambda_2 - \chi_i\right) \\ \vdots \\ \bar{a}_n / \left(\lambda_n - \chi_i\right) \end{bmatrix} \tag{2.36}
$$

and its norm is given by

$$
|\boldsymbol{\xi}_i^\star| = \sqrt{\left(\frac{a_1}{\lambda_1 - \chi_i}\right)^2 + \left(\frac{a_2}{\lambda_2 - \chi_i}\right)^2 + \ldots + \left(\frac{a_n}{\lambda_n - \chi_i}\right)^2} \; . \tag{2.37}
$$

As already demonstrated for large distances between the eigenvalues and with equation (2.34) the coordinates of $\boldsymbol{\xi}_i^\star$ can be approximated by

$$
\xi_{ij}^\star = \frac{a_j}{\lambda_j - \chi_i} \quad \text{for} \quad j < m \tag{2.38}
$$

respectively

$$
\xi_{ij}^\star = 0 \quad \text{for} \quad j > m \; . \tag{2.39}
$$

The length of $\boldsymbol{\xi}_i^\star$ is less affected by eigenvalues λ_j with large distance to χ_i, because here the squares of the reciprocals of the distances are computed. Thus looking at equation (2.31)

$$
\boldsymbol{\phi}_i = \begin{pmatrix} | & | & & | & & | \\ \boldsymbol{\psi}_1 & \boldsymbol{\psi}_2 & \ldots & \boldsymbol{\psi}_j & \ldots & \boldsymbol{\psi}_n \\ | & | & & | & & | \end{pmatrix} \boldsymbol{\xi}_i \tag{2.40}
$$

follows that the jth coordinate in vector $\boldsymbol{\xi}_i$ obviously represents the influence of the old modal vector $\boldsymbol{\psi}_j$ of $\boldsymbol{K}$ on the computation of the shifted eigenvector $\boldsymbol{\phi}_i$ due to the rank-1-update, which gives an a posteriori control for $\boldsymbol{\Xi}$: To estimate the accuracy of the eigenmodes $\boldsymbol{\phi}_i$ computed with a reduced set of m eigenvalues λ_j and -vectors $\boldsymbol{\psi}_j$ the modal factor matrix $\boldsymbol{\Xi}$ must be considered. In the case of a fully populated matrix the mutual influence of the eigenvectors is obviously high or the previous assumption $\bar{a}_j \ll \lambda_{m+1}$ was not correct, which means that a new computation with a larger set of eigenvalues λ_j and -vectors $\boldsymbol{\psi}_j$ is probably necessary. In the case of a less populated modal factor matrix with a dominantly diagonal shape, a new computation with a larger modal set would not affect the solution remarkably.

2.4   Multiple Rank updates

Although it may seem that the derived algorithm is only valid for a rank-one-update of the stiffness matrix $\boldsymbol{K}$, multiple rank updates can easily be taken into account by a subsequent application of this method. I. e. in the case of a closed chamber (see Fig. 1.1), which is partially filled with a heavy incompressible fluid and an additional gas volume the system matrix $\boldsymbol{A}$ in the equilibrium equations according to [9] features a rank-2-update:

$$
\boldsymbol{A} = \boldsymbol{K} + \alpha_t \left(\boldsymbol{a} + \boldsymbol{b}\right)\left(\boldsymbol{a} + \boldsymbol{b}\right)^T - \gamma_t \boldsymbol{b}\boldsymbol{b}^T \; , \tag{2.41}
$$

where α_t again couples the total volume change $\boldsymbol{a} + \boldsymbol{b}$ with the gas pressure change Δp^{kg} and the pressure volume gradient γ_t at time t couples the change of the fluid level $\Delta \boldsymbol{x}^o$ with the volume change $\boldsymbol{b}$ under the wetted shell surface. The formulae for the computation of $\boldsymbol{a}$, $\boldsymbol{b}$, α_t and γ_t are summarized in the appendix. To compute the eigenvalues and -vectors the stiffness matrix with the first rank update is split according to equation (2.41), which leads to a matrix $\boldsymbol{A}^1$ only affected by the gas volume change $(\boldsymbol{a} + \boldsymbol{b})$:

$$\boldsymbol{A}^1 = \boldsymbol{K} + \alpha_t \left(\boldsymbol{a} + \boldsymbol{b}\right)\left(\boldsymbol{a} + \boldsymbol{b}\right)^T \tag{2.42}$$

For this rank-one-update the eigenvalues and -vectors can be computed as described in the previous section. In the same manner the shift of eigenvalues and -vectors of $\boldsymbol{A}^1$ due to the second rank update can be computed.

$$\boldsymbol{A}^2 = \boldsymbol{A}^1 - \gamma_t \boldsymbol{b}\boldsymbol{b}^T \tag{2.43}$$

3 Numerical Examples

As shown in [9], the effects of a volume dependent gas or fluid loading on the system matrices can be summarized to:

- The global stiffness matrix $\boldsymbol{K}^{el}$ of the elastic shell structure is updated with the normal change parts [15] due to fluid $\boldsymbol{K}^f$ and gas $\boldsymbol{K}^g$ loading to: $\boldsymbol{K} = \boldsymbol{K}^{el} + \boldsymbol{K}^f + \boldsymbol{K}^g$.

- Further rank updates of $\boldsymbol{K}$ have to be considered due to the volume dependence of the gas/fluid support, see equations (2.1) and (2.41)

- At least within a nonlinear analysis with changing loading the right-hand-side vector $\boldsymbol{f}^{ex} - \boldsymbol{f}^{el}$ has to be updated because of the volume dependence of the gas/fluid support: $\boldsymbol{f} = \boldsymbol{f}^{ex} - \boldsymbol{f}^{el} - \boldsymbol{f}^f - \boldsymbol{f}^g$.

In section 2 an algorithm for an efficient eigenvalue and eigenmode extraction of the global system matrix was presented, also considering the dyadic rank updates due to volume coupling. As already shown these specific rank-updates lead to an eigenvalue shifting of the old eigenvalues λ to increased values χ.

In this section some numerical examples will be presented in order to discuss the influence of the fluid-structure-interaction on the stability behavior of thin-walled shell structures, especially the quantitative shifting of the eigenvalues and the coupling of the eigenmodes due to the volume dependence. The first examples will deal with fairly stiff structures under several loading conditions. Afterwards the inflation and hydrostatic loading of a rubber dam will serve as an example for soft structures showing large deformations.

3.1 Fairly stiff structures

This section deals with closed steel cylinders under the following loading conditions:

- empty cylinder

- gas loaded cylinder

- partially fluid filled cylinder

- partially fluid and gas filled cylinder

- completely fluid filled cylinder

As in the previous section in a first phase the internal fluid/gas support conditions are applied quasi statically and afterwards the axial loading – directly imposed on the upper cap – is steadily increased until the first eigenvalue equals zero and thus the critical buckling load is reached. The steel cylinder features a height of $h = 40 \ m$, a radius of $r = 20 \ m$ and a thickness ratio of $r/t = 1000$. The upper and lower caps are connected to the cylinder with a Navier support and modeled as nearly rigid bodies, to prevent the cap from buckling before the global buckling state is reached. In order to cover also unsymmetric buckling modes half of the cylinder instead of a quarter is used for the computation. For the discretization about 1400 linear solid shell [10] elements with ANS/EAS enhancements are taken. Table 1 provides an overview over all simulations:

Starting with the ***empty cylinder*** under axial loading – load case a) – a critical buckling load of $F_{crit} = 420 \ MN$ is achieved. Further on, the typical buckling mode with a high number of buckling waves along the lower boundary can be observed.
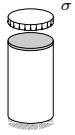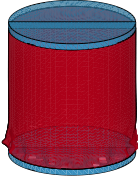
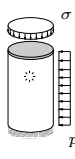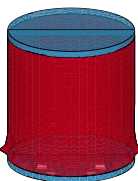For a ***gas filled cylinder*** with an internal gas pressure of $p^{kg} = 1 \ bar$ – load case b) – the buckling load is increased by a factor of 1.71 compared to the empty cylinder. The buckling mode shows less buckling waves as in the first case, but they are still concentrated along the lower boundary, see Table 1. Neglecting the volume dependence of the right-hand-side vector (pressure increase due to structural deformation: $\Delta p^{kg} = 0.2\%$) only slightly affects the critical buckling load. In Fig. 3.1 this correlation between the volume change due to deformation and the internal gas pressure – performed via the adiabatic state equation – is depicted.

The ***partially fluid filled cylinder*** with a maximum pressure amplitude of $p_{max} = 3.6 \ bar$ at the bottom – load case c) – has a critical buckling load of $600 \ MN$, which is about a factor 1.44 higher as for the empty cylinder. However, although the pressure amplitude is much higher in this case as for the gas filled cylinder, the buckling load is still 16% lower. This is due to the fact that the hydrostatic distribution is linear in contrast to the constant gas pressure distribution and only affects elements below a water level of $x^o = 36 \ m$. Further for the open cylinder a consideration of the volume dependence neither for the stiffness matrix nor for the right-hand-side vector leads to remarkable differences in the buckling load and the buckling mode. The buckling waves concentrate along the upper boundary, where the stiffening circumferential stresses show the lowest values.
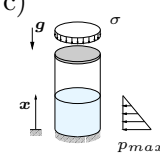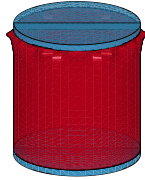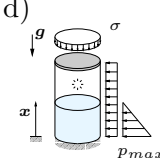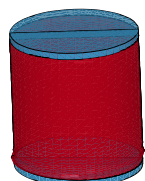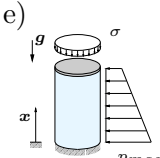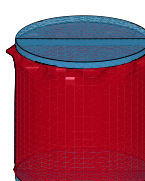
Starting with an initial gas pressure of $p^{kg} = 20 \ mbar$ and slowly increasing the interior water level (and thus decreasing the gas volume) to $x^o = 39 \ m$ results for the ***partially gas and fluid filled cylinder*** – load case d) – in a critical load, which is about a factor of 2.06 higher as for the empty cylinder. The maximum pressure amplitude at the end of the filling phase is $p_{max} = 5.6 \ bar$. Neglecting the volume dependence of the right-hand-side during the filling phase would only result in a maximum pressure amplitude of $p_{max} = p^{kg} + \rho g x^o \approx 3.9 \ bar$ and thus leads to a considerably lower estimate of the buckling load. The structural displacements caused by the axial loading lead to a further pressure increase of $0.3 \ bar$. Hence, beginning the analysis directly (without simulating the filling process) with an already filled cylinder and with a comparable pressure amplitude of $p_{max} = 5.6 \ bar$

would only slightly affect the critical buckling load. Due to the relatively high internal pressure the cylinder behaves almost as a rigid body and shows a kind of beam-like shear buckling in combination with an elephant foot buckling along the lower boundary.

The last case is a ***completely fluid filled cylinder*** under axial loading – load case e). In comparison with the empty cylinder the buckling load F_{crit} of the fluid filled cylinder is about a factor 2.17 higher. The buckling mode clearly shows high frequency buckling waves along the upper edge and an elephant-foot type buckling wave along the lower boundary. A surprising fact is that although the almost same pressure amplitude and pressure distribution as in the case of the partially fluid and gas filled cylinder are acting, the buckling modes are different. But looking at the higher eigenvalues shows that in the critical buckling state the 2nd and 3rd eigenvalue (which corresponds to the beam-like shear buckling mode similar to the gas+fluid filled cylinder) are also very close to zero. Thus already a slight change in the pressure amplitude might have led to the same beam-like shear buckling mode as in the previous example. The axial loading, starting at load step 20 (current over-pressure amplitude of $p_{max} = 4.0$ *bar*), leads to a slight fluid volume compression of about 0.04%. In Fig. 3.2 the relation between volume change and density change is depicted. Despite the fact that this volume change is relatively small, it leads to very high internal pressure if the bulk modulus of the fluid is chosen to be that of water with $K = 0.5 \cdot 10^3 N/mm^2$. Fig. 3.3 depicts the development of the compressible pressure part p_t^{kf} during the loading process. This pressure increase from 3 *bar* to 5.3 *bar* (leading to $p_{max} = 6.3$ *bar*) due to structural displacements is responsible for a buckling load, which is about 32% higher compared to a computation of F_{crit} neglecting the volume dependence of the right-hand-side.

Load case	p_{max}	Δp	Buckling mode	Remarks
a)	0 bar			• $F_{crit} = 420MN$ • buckling starts at lower boundary • high number of buckling waves
b)	1.0 bar	0.2 bar		• $F_{crit}/F_{crit}^{empty} = 1.71$ • buckling mode with less waves • small differences in F_{crit} if $RHS \neq \boldsymbol{f}(\Delta v)$

(To be continued on next page)

c)
 	
	3.6 bar	0 bar		• $F_{crit}/F_{crit}^{empty} = 1.44$
				• buckling starts
				  at upper boundary
				• high number
				  of buckling waves

d)
 	
	5.6bar	0.3 bar		• $F_{crit}/F_{crit}^{empty} = 2.06$
				• beam-like shear buck-
				  ling and elephant foot
				  buckling
				• -30% difference in
				  F_{crit} if $RHS \neq \boldsymbol{f}(\Delta v)$
				  (if filling process is considered)

e)
 	
	4.0 bar	2.3 bar		• $F_{crit}/F_{crit}^{empty} = 2.17$
				• buckling along upper edge
				  and elephant foot
				  buckling along lower edge
				• -32% difference in
				  F_{crit} if $RHS \neq \boldsymbol{f}(\Delta v)$

Table 3.1: Stability analyses of closed cylinder under axial loading with different internal pressure configurations

Discussion

The previous examples showed that the internal gas/fluid pressures lead to high circumferential stresses. This hydrostatic pretensioning of the cylinders dominates the solution and therefore leads to considerably higher buckling loads in comparison to the empty cylinder. Depending on the pressure amplitude and the pressure distribution (constant or linear) the buckling modes also differ considerably.

But as already mentioned, in the cases of the steel cylinders considering the left-hand-side parts (stiffness matrix terms) of the volume coupling both in the equilibrium iterations and in the stability computation did not affect the solution to a high degree. Inspecting the modal factor matrix $\boldsymbol{\Xi}$ makes clear that there is almost no coupling between the old eigenvectors (computed without rank-update) and the new eigenvectors, because it is almost identical to the identity matrix $\boldsymbol{I}$. Thus for fairly stiff structures the rank-updates of the left-hand-side are negligible. On the other hand the examples showed that, although the volume changes were small, neglecting also the volume dependence of the right-hand-side vector resulted in different buckling loads for the same load case. Therefore at least the right-hand-side should be updated with the volume dependent information to achieve realistic results.
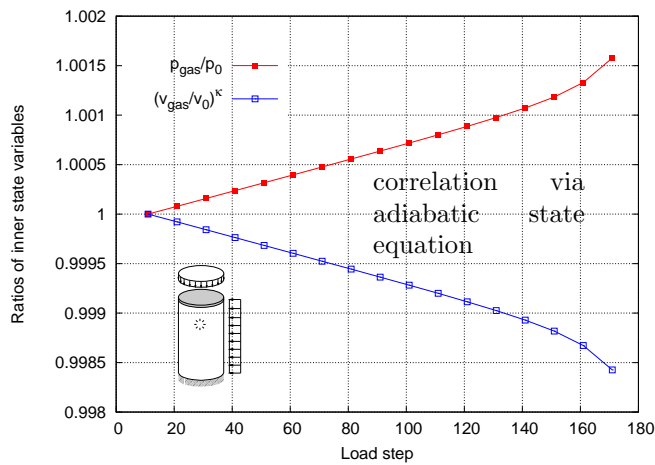
Fig. 3.1: Distribution of inner state variables during complete loading process
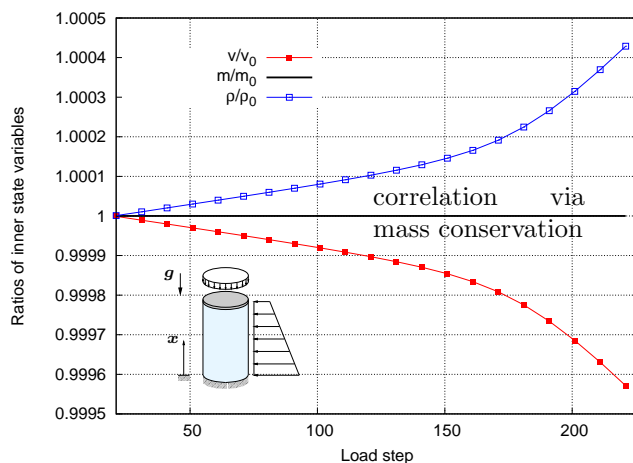

Fig. 3.2: Distribution of inner state variables during loading process

3.2 Soft structures

After investigating fairly stiff structures the effect of the volume dependence on the eigenvalues and eigenmodes of the global system matrix will now be investigated for soft structures. The inflation and hydrostatic loading of a rubber dam will serve as a real world example for a multi chamber system with varying loading conditions; hydrodynamic effects will not be considered in these examples. For a discussion of the general application of such dams is referred to [7]. The rubber dam consists of two fiber reinforced membrane parts (thickness $t = 30\ mm$, width $w = 3.20\ m$, length $l = 19\ m$, Young's modulus $E = 60\ N/mm^2$, Poisson ratio $\nu = 0.4$), which are hot vulcanized along one edge resulting in the typical deflection fin, which later is helpful to reduce vibrations. Along the other edge the two membrane layers are clamped and anchored to the ground. The most important task of such controlled dams is the adjustment of the water retention level resp. the dam height, which allows to take control of the discharge. In the case of inflatable dams the dam height h can
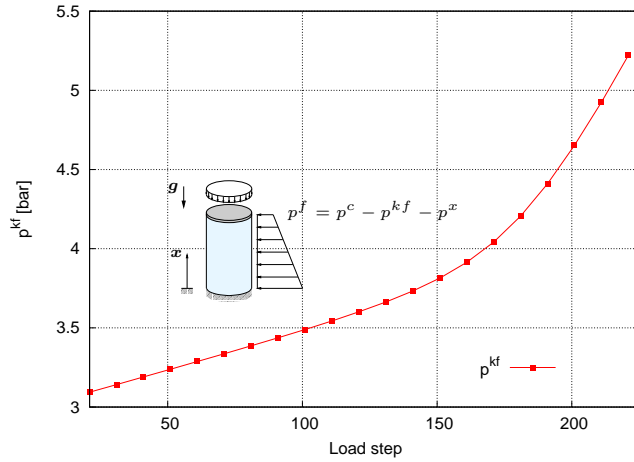
Fig. 3.3: Development of pressure p^{kf} due to volume compression during loading process

be simply regulated by the internal gas pressure. Characteristic for gas filled rubber dams is a typical buckling mode, the so-called V-notch (see Fig. 3.5a), which already appears at relatively low head water levels, depending on the bending stiffness of the dam membrane and the incident flow. The computation is performed in several steps: First the membrane structure is deployed by increasing the internal pressure. Afterwards the head water levels will be raised. In this special load case with head water loading and an interior gas filling a 2-chamber system is the appropriate analysis model. Although the head water level is not affected by the deformation of the dam, (resulting only in a rank-1-update of the stiffness matrix due to volume dependence of the gas filling), the normal change parts and the residual vectors for all 2 chambers have to be considered. For reasons of symmetry only half of the dam model is discretized using about 1300 solid-shell elements [10] with linear shape functions and ANS/EAS enhancements for the kinematics. The dam is clamped along one edge; along the bottom a pure penalty contact model is chosen. One end of the dam is left free while the other end features the symmetry boundary conditions. After the inflation process of the dam is finished, its free end is now fixed by a penalty contact in horizontal direction to simulate the real world boundary condition, see Fig. 3.5a). Fig. 3.4 presents some information on the equilibrium iterations necessary for a load step together with the maximum value of the circumferential strain $\varepsilon_{\varphi\varphi}$. While in the first load step the contact formulation and the volume change of the dam body cause a high number of iterations, the perfect matching of the development of the strains and the iteration number demonstrate that in the following load steps the inner forces dominate the number of equilibrium iterations. With increasing internal pressure the inner forces are also steadily increased leading in combination with large volume changes and large shell rotations to a high number of iterations during the inflation process. From load step 25 on the rise of the head water level slightly reduces the inner forces again and thus the number of equilibrium iterations decreases too. At the end the heavy water loading becomes too high and forces the dam to perform a kind of rolling motion leading again to large strains and thus high iteration numbers. In Fig. 3.5 the typical V-notch buckling mode of a real world dam under hydrostatic loading is depicted in comparison to the eigenmode computed with
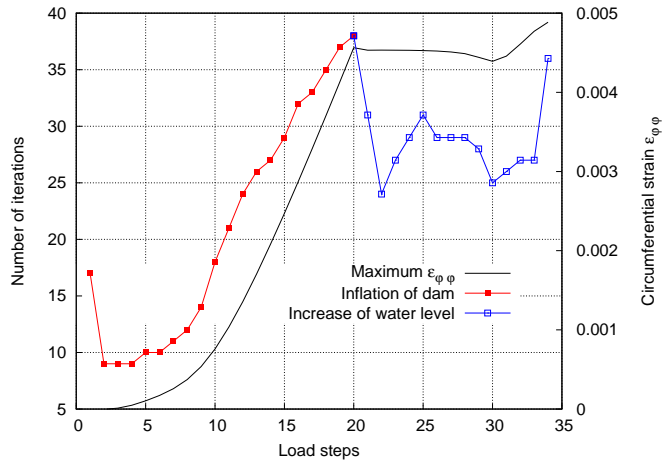
Fig. 3.4: Inflation and loading of rubber dam: Number of iterations per load step

a)   b)
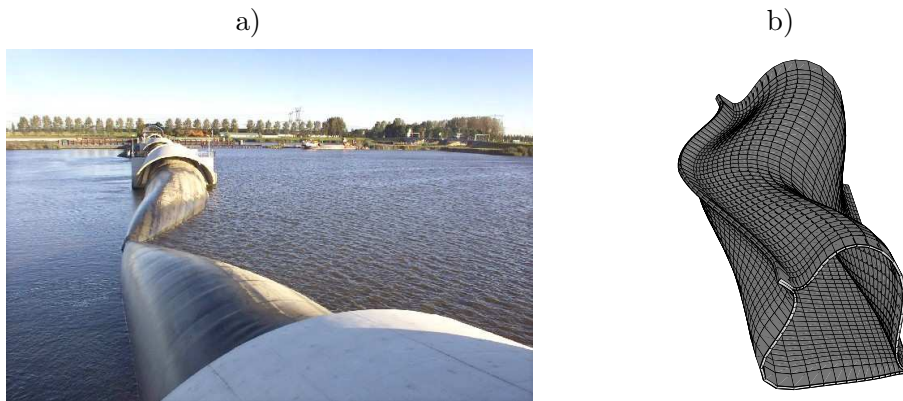
Fig. 3.5: a) Real world buckling mode and b) FE eigenmode of inflatable dam under hydrostatic loading

the presented FE algorithm. From the numerical side the more interesting fact is the population of the modal factor matrix $\mathbf{\Xi}$, which is shown in Fig. 3.6 for several load steps. In section 3.1 for fairly stiff structures the modal factor matrix was almost the identity matrix. For soft structures the modal factor matrices in Fig. 3.6 show a clear coupling between the eigenmodes. In the first few load steps, when the system is still low pressurized and almost without any stiffness the coupling is most visible. A strong coupling between the last four eigenmodes can be observed in load step 5 (participation between 10% and 100%). For the almost fully pressurized dam (load steps 15-20) the high internal forces dominate the global stiffness matrix, resulting in a weakly populated modal factor matrix and thus a decoupling of the eigenmodes. The hydrostatic (load steps 30-34) loading activates the coupling again, with participation values of the eigenmodes between 1% and 10%. In Fig. 3.7 the eigenvalue shifting due to volume coupling – calculated by the ratio of the shifted eigenvalue χ_1 to the original eigenvalue λ_1 – during the loading process is depicted. Similar to the coupling of the eigenmodes for a low pressurized very soft structure (load steps 1-5) the effect of the volume dependence (resp. the dyadic rank-update
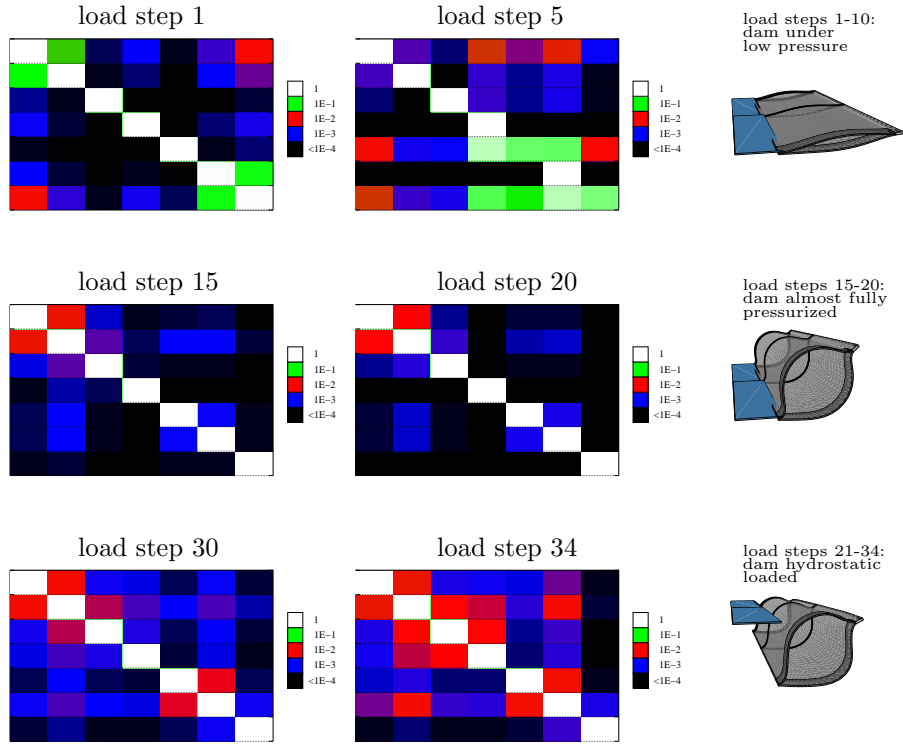
Fig. 3.6: Rubber dam: Population of modal factor matrix $\boldsymbol{\Xi}$ during loading process

structural stiffness matrix $\boldsymbol{A} = \boldsymbol{K} + \boldsymbol{a}\boldsymbol{a}^T$) becomes dominant: The first eigenvalue χ_1 of $\boldsymbol{A}$ is about 35% higher compared to the eigenvalue λ_1 of $\boldsymbol{K}$. For higher pressures the increasing internal forces then prevail the stiffening effect of the rank-update on the eigenvalues, visible in the constant relatively low rate for the eigenvalue change. Only in the last load steps when the water level equals the dam height, changes up to 5% can be observed again.

4   Conclusions

This contribution contains investigations of the influence of gas or fluid support on the eigenvalues and eigenmodes of the stiffness matrix of shell or membrane-like structures undergoing large displacements. The derived equations consider the change of the inner state variables (e.g. the gas pressure p^{kg}) during the deformation process depending on volumetric effects as e.g. a closed containment. This leads to a stiffness matrix, with additional dyadic updates, which allowed the derivation of an efficient algorithm to compute the eigenvalues and eigenmodes just by shifting the old eigenvalues. The effect of the gas or fluid support is reflected in the coordinates of the modal factor matrix: For a nearly unaffected system (as in the case of the gas supported steel cylinder) it has approximately the shape of the identity matrix. In the case of the soft membrane structure, it is at least in the low pressurized state and the final inflated and hydrostatic loaded state fully occupied by non-zero entries, thus leading to slightly different eigenmodes compared to the original modes.
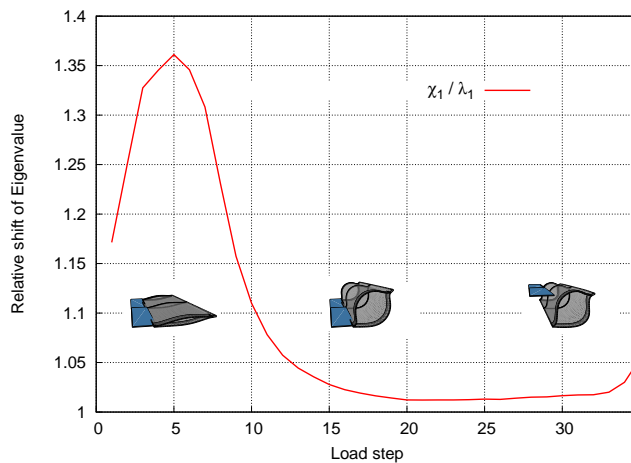
Fig. 3.7: Rubber dam: Development of relative eigenvalue change due to volume coupling during loading process

The examples showed that for a modal analysis in the case of soft, low pressurized structures a consideration of the volume dependence of the gas/fluid support is important, because here the structure is gaining a certain amount of additional stiffness. For stiffer structures however, the effect of the volume dependence on the eigenvalues and eigenmodes is negligible and therefore the modal analysis can be performed with conventional algorithms neglecting the rank-updates. Nevertheless the example with the partially gas+fluid filled cylinder and the completely fluid filled cylinder showed that at least for the computation of the right-hand-side the volume dependence should be taken into account.

5 Appendix – Nomenclature and formulae

For a detailed description see also [9].

- ^{g}, ^{f} Indices denoting the area of structural surface wetted with gas resp. fluid
- $_t$ Index denoting the current state t in the linearization
- ξ, η and $\bar{\xi}$, $\bar{\eta}$ Co- and contravariant coordinates
- $\boldsymbol{e}_\xi \otimes \boldsymbol{e}_\eta$ and $\boldsymbol{e}^{\bar{\xi}} \otimes \boldsymbol{e}^{\bar{\eta}}$ Co- and contravariant base systems
- $\boldsymbol{N}(\xi,\eta)$ Isoparametric shape functions of finite element surfaces
- $\boldsymbol{g}$ Acceleration of gravity
- $\boldsymbol{n} = \boldsymbol{e}_\xi \times \boldsymbol{e}_\eta$ Non-normalized normal vector on surface
- ρ Fluid density
- p^{kg}, p^{kf} Gas and fluid pressure due to volume compression
- $p^x = \rho \boldsymbol{g} \cdot \boldsymbol{x}$ Hydrostatic pressure at structural surface point $\boldsymbol{x}$
- $p^c = \rho \boldsymbol{g} \cdot \boldsymbol{c}$ Hydrostatic pressure in the center of gravity $\boldsymbol{c}$

of the fluid

- $p^o = \rho \boldsymbol{g} \cdot \boldsymbol{x}^o$ Hydrostatic pressure resulting from free fluid surface level $\boldsymbol{x}^o$

- $\bar{v}^g, \bar{v}^f$ Gas and fluid volume

- $\bar{v}_0^f$ Initial fluid volume

- Γ^o Free fluid surface

- $\alpha = \kappa p^{kg}/\bar{v}^g, \quad \beta = K/\bar{v}_0^f, \quad \gamma = \rho|\boldsymbol{g}|/\Gamma^o$ Pressure volume gradients

- $\bar{\alpha} = \alpha/(\alpha + \beta), \bar{\beta} = \beta/(\alpha + \beta)$ stiffness parameters defining load case (see [9])

- $p^f = (1 - \bar{\beta})\, p^c - (1 - \bar{\beta})\, p^{kf} - \bar{\beta} p^{kg} + \bar{\beta} p^o - p^x$ Absolute fluid pressure

- $p^g = \bar{\alpha}\, (p^c - p^o) - (1 - \bar{\alpha})\, p^{kg} - \bar{\alpha} p^{kf}$ Absolute gas pressure

- $\boldsymbol{W}^{\bar{\xi}} = \boldsymbol{n}_t \otimes \boldsymbol{e}^{\bar{\xi}} - \boldsymbol{e}^{\bar{\xi}} \otimes \boldsymbol{n}_t , \quad \boldsymbol{W}^{\bar{\eta}} = \boldsymbol{n}_t \otimes \boldsymbol{e}^{\bar{\eta}} - \boldsymbol{e}^{\bar{\eta}} \otimes \boldsymbol{n}_t$
              Skew symmetric contravariant tensors

- Load-stiffness matrices due to the change of the normal of the wetted surfaces

    - *Gas*

    $$\boldsymbol{K}_{elem}^g = \frac{1}{2} \int_{\eta^g} \int_{\xi^g} p_t^g \begin{pmatrix} \boldsymbol{N} \\ \boldsymbol{N}_{,\xi} \\ \boldsymbol{N}_{,\eta} \end{pmatrix}^T \begin{pmatrix} \boldsymbol{0} & \boldsymbol{W}^{\bar{\xi}} & \boldsymbol{W}^{\bar{\eta}} \\ \boldsymbol{W}^{\bar{\xi}T} & \boldsymbol{0} & \boldsymbol{0} \\ \boldsymbol{W}^{\bar{\eta}T} & \boldsymbol{0} & \boldsymbol{0} \end{pmatrix} \begin{pmatrix} \boldsymbol{N} \\ \boldsymbol{N}_{,\xi} \\ \boldsymbol{N}_{,\eta} \end{pmatrix} d\xi d\eta \,,$$

    - *Fluid*

    $$\boldsymbol{K}_{elem}^f = \frac{1}{2} \int_{\eta^f} \int_{\xi^f} p_t^f \begin{pmatrix} \boldsymbol{N} \\ \boldsymbol{N}_{,\xi} \\ \boldsymbol{N}_{,\eta} \end{pmatrix}^T \begin{pmatrix} \boldsymbol{0} & \boldsymbol{W}^{\bar{\xi}} & \boldsymbol{W}^{\bar{\eta}} \\ \boldsymbol{W}^{\bar{\xi}T} & \boldsymbol{0} & \boldsymbol{0} \\ \boldsymbol{W}^{\bar{\eta}T} & \boldsymbol{0} & \boldsymbol{0} \end{pmatrix} \begin{pmatrix} \boldsymbol{N} \\ \boldsymbol{N}_{,\xi} \\ \boldsymbol{N}_{,\eta} \end{pmatrix} d\xi d\eta$$
    $$- \frac{\rho_t}{2} \int_{\eta^f} \int_{\xi^f} \boldsymbol{N}^T \left(\boldsymbol{n}_t^f \otimes \boldsymbol{g} + \boldsymbol{g} \otimes \boldsymbol{n}_t^f \right) \boldsymbol{N} \; d\xi d\eta \,,$$

- Load vectors due to gas and fluid pressure loading

    $$\boldsymbol{f}_{elem}^g = \int_{\eta^g} \int_{\xi^g} \left[\bar{\alpha}\, (p_t^c - p_t^o) - (1 - \bar{\alpha}) p_t^{kg} - \bar{\alpha} p_t^{kf} \right] \boldsymbol{N}^T \boldsymbol{n}_t^g \; d\xi d\eta$$

    $$\boldsymbol{f}_{elem}^f = \int_{\eta^f} \int_{\xi^f} \left[(1 - \bar{\beta})\, p_t^c - (1 - \bar{\beta}) p_t^{kf} - \bar{\beta} p_t^{kg} + \bar{\beta} p_t^o - p_t^x \right] \boldsymbol{N}^T \boldsymbol{n}_t^f \; d\xi d\eta$$

- Coupling vectors for gas and fluid parts

    $$\boldsymbol{a}_{elem} = \int_{\eta^g} \int_{\xi^g} \boldsymbol{N}^T \boldsymbol{n}_t^g \; d\xi d\eta \,, \qquad \boldsymbol{b}_{elem} = \int_{\eta^f} \int_{\xi^f} \boldsymbol{N}^T \boldsymbol{n}_t^f \; d\xi d\eta$$

References

[1] H. D. Baehr. *Thermodynamik*. Springer-Verlag Berlin, 2005.

[2] D. Berry and H. Yang. Formulation and experimental verification of a pneumatic finite element. *International Journal for Numerical Methods in Engineering*, 39:1097–1114, 1996.

[3] J. Bonet, R. D. Wood, J. Mahaney, and P. Heywood. Finite element analysis of air supported membrane structures. *Computer Methods in Applied Mechanics and Engineering*, 190:579–595, 2000.

[4] R. van Dijk, F. van Keulen, and J. Sterk. Simulation of closed thin-walled structures partially filled with fluid. *International Journal of Solids and Structures*, 37:6063–6083, 2000.

[5] J. D. Faires and R. L. Burden. *Numerische Methoden*. Spektrum Akademischer Verlag, 1994.

[6] Y. Fung and E. Sechler. Buckling of thin-walled circular cylinders under axial compression and internal pressure. *Journal of Aeronautical Sciences*, 24:351–356, 1957.

[7] M. Gebhardt. *Hydraulische und statische Bemessung von Schlauchwehren*. PhD thesis, Institut für Wasserwirtschaft und Kulturtechnik der Universität Karlsruhe (TH), 2006.

[8] L. Harris et al. The stability of thin-walled unstiffened circular cylinders under axial compression including the effects of internal pressure. *Journal of Aeronautical Sciences*, 24:587–596, 1957.

[9] M. Haßler and K. Schweizerhof. On the interaction of fluid and gas loaded multichamber systems in a large deformation finite element analysis. *(Submitted for publication)*, 2006.

[10] R. Hauptmann and K. Schweizerhof. A systematic development of 'solid-shell' element formulations for linear and non-linear analysis employing only displacement degrees of freedom. *International Journal for Numerical Methods in Engineering*, 42:49–69, 1998.

[11] T. Rumpel and K. Schweizerhof. Volume-dependent pressure loading and its influence on the stability of structures. *International Journal for Numerical Methods in Engineering*, 56:211–238, 2003.

[12] T. Rumpel and K. Schweizerhof. Hydrostatic fluid loading in non-linear finite element analysis. *International Journal for Numerical Methods in Engineering*, 59:849–870, 2004.

[13] T. Rumpel, K. Schweizerhof, and M. Haßler. Efficient finite element modelling and simulation of gas and fluid supported membrane and shell structures. *Recent Advances in Textile Membranes and Inflatable Structures,E. Onate, B. Kröplin (eds.)*, 2004.

[14] K. Schweizerhof. *Quasi-Newton Verfahren und Kurvenverfolgungsalgorithmen für die Lösung nichtlinearer Gleichungssysteme in der Strukturmechanik*. Institut für Baustatik der Universität Karlsruhe (TH), 1989.

[15] K. Schweizerhof and E. Ramm. Displacement dependent pressure loads in nonlinear finite element analyses. *Computers and Structures*, 18:1099–1114, 1984.